Journal of Materials Chemistry A

PAPER

View Article Online
View Journal | View Issue

Cite this: *J. Mater. Chem. A*, 2017, **5**, 10632

1-D nanostructure comprising porous Fe_2O_3/Se composite nanorods with numerous nanovoids, and their electrochemical properties for use in lithium-ion batteries†

Jung Sang Cho,[ab] Jin-Sung Park,[a] Kyung Min Jeon[a] and Yun Chan Kang*[a]

Received 25th March 2017
Accepted 2nd May 2017

DOI: 10.1039/c7ta02616a

rsc.li/materials-a

Novel 1-D nanostructures composed of porous Fe_2O_3/Se composite or subsequently formed hollow Fe_2O_3 nanorods were introduced. Carbon nanofibers embedded with $FeSe_2$ needle-like nanorods were prepared *via* the selenization of electrospun nanofibers. During the oxidation process, the faster diffusion rate of Fe ions (76 pm in size) relative to that of the Se ions (184 pm in size) resulted in nanoscale Kirkendall diffusion mechanism, thus forming the 1-D nanostructure comprising nanorods composed of Se/voids/Fe_2O_3 as an intermediate. The complete conversion of $FeSe_2$ into Fe_2O_3 and the combustion of C, which caused necking between the nanorods, resulted in a 1-D nanoarchitecture composed of hollow Fe_2O_3 nanorods. The discharge capacity during the 400th cycle of the 1-D nanostructures comprising Fe_2O_3/Se composite nanorods was 1456 mA h g^{-1} at a current density of 1.0 A g^{-1}. The high structural stability of this unique architecture during repeated lithium insertion/deinsertion processes resulted in superior lithium-ion storage performance.

Introduction

Over the past decade, porous and hollow nanomaterials with various morphologies and compositions have been developed for widespread applications in energy storage, catalysis, gas sensors, drug delivery, and hydrogen evolution reaction.[1–5] Among these, one-dimensional (1-D) nanostructures exhibiting unique electrical, optical, and magnetic properties have matured considerably for these potential applications.[6–10]

For Li-ion battery (LIB) applications in particular, 1-D nanomaterials offer several advantages over other higher-dimensional nanomaterials such as enhanced surface-to-volume ratios and efficient 1-D electron transport along the longitudinal direction, which enable the materials to interact more efficiently with Li^+ ions.[10–15] Additionally, the introduction of hollow and porous structures into 1-D nanomaterials decreases the ion diffusion length and increases the contact area between the electrolyte and electrode for Li^+ insertion/deinsertion.[15–19] These structures can accommodate volume changes during cycling, resulting in excellent electrochemical properties.[15–19]

In these contexts, various 1-D nanomaterials with hollow or porous structures have been developed as efficient anode materials for LIBs with good electrochemical performance.[15,20–24] Cho *et al.* exploited the Kirkendall effect to synthesize bubble-nanorod-structured nanofibers composed of hollow Fe_2O_3 nanospheres uniformly dispersed in a C matrix. The nanofibers exhibited a discharge capacity of 812 mA h g^{-1} during the 300th cycle at a high current density of 1.0 A g^{-1}.[15] Hong *et al.* introduced fiber-in-tube-structured SnO_2 nanofibers with a fiber@void@tube configuration, which improved the electrochemical properties by reducing the diffusion length of the Li^+ ions and improving the structural stability of the nanotubes during cycling.[21] Yu *et al.* also fabricated a Sn/C composite structure, namely, Sn@C encapsulated in bamboo-like hollow C nanofibers, which displayed a high reversible capacity of 737 mA h g^{-1} after 200 cycles at 0.5C.[24]

Among the transition metal oxides, Fe_2O_3 has attracted considerable interest as an anode material for LIBs in recent years because of its high capacity, low cost, and environmental friendliness.[25–29] Unfortunately, Fe_2O_3 exhibits low reversible capacities and frustrating cycle performance due to its low intrinsic electronic conductivity and large volume expansion during cycling.[25–29] Therefore, many strategies devoted to improving Fe_2O_3 anode materials are under development.[15,26–29] Despite these efforts, the electrochemical properties of Fe_2O_3 remain unsatisfactory for LIB applications.

In this study, we propose for the first time two novel hierarchical 1-D nanostructures, one comprising porous Fe_2O_3/Se

[a]*Department of Materials Science and Engineering, Korea University, Anam-Dong, Seongbuk-Gu, Seoul 136-713, Republic of Korea. E-mail: yckang@korea.ac.kr; Fax: +82-2-928-3584*

[b]*Department of Engineering Chemistry, Chungbuk National University, Chungbuk 361-763, Republic of Korea*

† Electronic supplementary information (ESI) available. See DOI: 10.1039/c7ta02616a

composite and the other comprising hollow Fe_2O_3 nanorods, prepared by a conventional electrospinning process and by exploiting a nanoscale Kirkendall diffusion mechanism. The formation mechanism of the hierarchical 1-D nanostructure was investigated in detail by tracing the changes in the nanofiber morphologies induced by a post-treatment. We expected that during cycling, the metalloid Se and the resulting $FeSe_x$ formed during the charging process would improve the electrical conductivity of the hierarchical 1-D nanostructure composed of porous Fe_2O_3/Se composite nanorods.

Experimental

One-dimensional nanostructures comprising porous Fe_2O_3/Se composite or hollow Fe_2O_3 nanorods were prepared using electrospinning and a two-step thermal-treatment process. First, iron(III) acetylacetonate ($Fe(acac)_3$)–polyacrylonitrile (PAN) composite nanofibers were electrospun as precursors. The electrospinning precursor solution was prepared by dissolving $Fe(acac)_3$ (6.0 g, STREM Chemicals, 99%) and PAN (4.0 g, Sigma-Aldrich, M_w: 150 000 g mol^{-1}) in *N*,*N*-dimethylformamide (60 mL, DMF, Sigma-Aldrich, 99%) with vigorous stirring overnight. The prepared solution was loaded into a plastic syringe equipped with a 25-gauge stainless steel nozzle. The solution was subsequently ejected at a flow rate of 2 mL h^{-1} and electrospun onto a drum collector covered with aluminum foil. During the electrospinning process, the distance between the tip and the collector was maintained at 20 cm, while the rotation of the drum was maintained at 100 rpm. The applied voltage between the collector and the syringe tip was 20 kV. The resulting $Fe(acac)_3$–PAN composite nanofibers were stabilized at 120 °C under air for 5 h. Subsequently, the initial post-treatment step to selenize the nanofibers was conducted at 400 °C for 6 h under H_2Se gas. During the selenization process, the $Fe(acac)_3$–PAN composite nanofibers and commercial Se metal powders were loaded into a covered alumina boat and placed in a quartz tube reactor. H_2 gas flew into the reactor, which reacted with the Se metal powders to form H_2Se gas. The selenization step resulted in the formation of $FeSe_2$–C composite nanofibers. Subsequently, the nanofibers were oxidized under an air atmosphere at 400, 500, or 600 °C for 3 h. For simplicity, the 1-D nanostructures composed of Fe_2O_3/Se or Fe_2O_3 nanorods obtained after oxidation at 400, 500, and 600 °C are referred to as "Sel.400-Oxi.400," "Sel.400-Oxi.500," and "Sel.400-Oxi.600," respectively.

The hierarchical Fe_2O_3 nanofibers with and without metalloid Se were observed by field emission scanning electron microscopy (FE-SEM, S-4800, Hitachi) and field emission transmission electron microscopy (FE-TEM, JEM-2100F, JEOL). In addition, their crystal phases were evaluated by X-ray diffractometry (XRD, X'Pert PRO MPD, PANalytical) using Cu Kα radiation ($\lambda = 1.5418$ Å) at the Korea Basic Science Institute (Daegu). X-ray photoelectron spectroscopy (XPS, Thermo Scientific K-Alpha™) with a focused monochromatic Al Kα beam at 12 kV and 20 mA was used to analyze the composition of the specimens. The surface areas of the nanofibers were measured using the Brunauer–Emmett–Teller (BET) method, using N_2 as the adsorbate gas. Thermogravimetric (TG) analysis was performed using a Pyris 1 TGA (PerkinElmer) at 25–650 °C with a heating rate of 10 °C min^{-1} under air.

The electrochemical properties of the hierarchical Fe_2O_3 nanofibers with and without metalloid Se were analyzed by constructing a 2032-type coin cell. The anode was prepared by mixing the active material, carbon black, and sodium carboxymethyl cellulose (CMC) at a weight ratio of 7 : 2 : 1. Li metal and microporous polypropylene film were used as the counter electrode and the separator, respectively. The electrolyte was composed of 1 M $LiPF_6$ dissolved in a mixture of fluoroethylene carbonate and dimethyl carbonate (FEC/DMC; 1 : 1 v/v). The discharge/charge characteristics of the samples were investigated by cycling over a potential range of 0.001–3 V at various current densities. Cyclic voltammograms (CV) were measured at a scan rate of 0.07 mV s^{-1}. The Fe_2O_3-containing negative electrode measured 1.5 cm × 1.5 cm, and the mass loading was approximately 1.5 mg cm^{-2}. Electrochemical impedance spectroscopy (EIS, ZIVE SP1) was performed over an alternating current frequency range of 0.01 Hz to 100 kHz.

Results and discussion

Two one-dimensional (1-D) nanostructures, one comprising porous Fe_2O_3/Se composite and the other comprising hollow Fe_2O_3 nanorods, were prepared by applying a two-step post-treatment process to the electrospun nanofibers. The formation mechanism for both types of 1-D nanostructure is described in Scheme 1. The precursor nanofibers composed of $Fe(acac)_3$ and PAN were prepared by an electrospinning process (Scheme 1-①). Then, Fe_3O_4–PAN nanofibers were obtained by stabilizing the as-spun nanofibers. The first post-treatment, *i.e.*, the selenization process, produced C nanofibers with embedded needle-like $FeSe_2$ nanorods (Scheme 1-②). The nucleation and subsequent longitudinal growth of $FeSe_2$ nanocrystals from Fe_3O_4 occurred all over the C matrix during

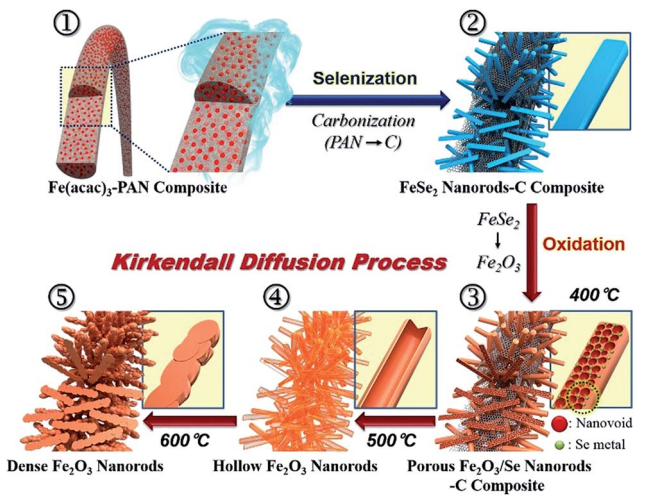

Scheme 1 Formation mechanism of the 1-D nanostructure comprising porous Fe_2O_3/Se composite and subsequent hollow Fe_2O_3 nano-rods by nanoscale Kirkendall diffusion.

the selenization process. During this stage, a large amount of C formed from PAN, which interfered with the crystal growth of the $FeSe_2$ nanorods by surrounding the $FeSe_2$ nanocrystals. During the second post-treatment, which was conducted under an air atmosphere, the $FeSe_2$–C composite nanofibers were oxidized to produce the porous Fe_2O_3/Se composite and the hollow Fe_2O_3 nanorod nanostructures at 400 and 500 °C, respectively (Scheme 1-③ and ④). A nanoscale Kirkendall diffusion mechanism occurred during the oxidation process. The oxidation of the $FeSe_2$ nanorods in the C matrix at a relatively low temperature of 400 °C produced porous Fe_2O_3/Se nanorods with numerous nanovoids *via* Kirkendall diffusion process (Scheme 1-③). Fe cation and Se anion diffused outwards more rapidly than oxygen diffused inwards. Additionally, the faster diffusion rate of Fe ions (76 pm in size) relative to that of the Se ions (184 pm in size) resulted in nanorods composed of $FeSe_2/Fe_2O_3$, Se/Fe_2O_3, and Se/nanovoids/Fe_2O_3, step by step. Therefore, Kirkendall nanovoids were simultaneously generated near the Se/Fe_2O_3 interfaces in the structure during the vacancy-assisted exchange of the material *via* bulk interdiffusion, which gave rise to coarsening and the enhancement of pore growth in the nanorods (Scheme 1-④). During this stage, the C between the nanorods in the structure decomposed into CO_2 gas. Eventually, $FeSe_2$ completely converted into Fe_2O_3 through a metalloid Se intermediate and the combustion of C, causing necking between the Fe_2O_3 nanorods and resulting in the 1-D nanostructure comprising hollow Fe_2O_3 nanorods (Scheme 1-④), as described in Scheme 1. Finally, the hollow nanorods transformed into Fe_2O_3 nanorods with filled structure *via* sintering at a high oxidation temperature of 600 °C (Scheme 1-⑤).

The formation mechanism of the porous Fe_2O_3/Se composite and hollow Fe_2O_3 nanorod nanostructures was investigated through the morphological changes induced by post-treatment in the composite nanofibers composed of $Fe(acac)_3$ and PAN. The nanofibers stabilized at 120 °C under an air atmosphere showed smooth surface structure with low-crystallinity Fe_3O_4 phase (Fig. S1†) and were transformed into a 1-D nanostructure with a uniquely hierarchical structure after selenization at 400 °C, as shown in Fig. 1. The low-crystallinity Fe_3O_4 phase and PAN constituting the nanofibers transformed into $FeSe_2$ and C, respectively, during the selenization process, as confirmed by XRD (Fig. 1b). As outlined previously in Scheme 1, numerous needle-like $FeSe_2$ nanorods were formed all over the C matrix during selenization, as indicated by the arrows in Fig. 1a. Although the selenization process was carried out at 400 °C, $FeSe_2$ nanocrystals formed and grew in the longitudinal direction, resulting in $FeSe_2$ nanorods. The $FeSe_2$ nanorods did not coarsen because the C surrounding the $FeSe_2$ disturbed the crystal growth of the nanorods.

In order to initiate the nanoscale Kirkendall diffusion mechanism, a second post-treatment step to oxidize the $FeSe_2$–C composite was carried out at 400, 500, or 600 °C under an air atmosphere. The conversion of $FeSe_2$ into Fe_2O_3 occurred during the oxidation process, which was confirmed by XRD (Fig. S2†). By applying the Scherrer's equation to the (104) crystal plane of the hexagonal Fe_2O_3 peak, the mean crystallite

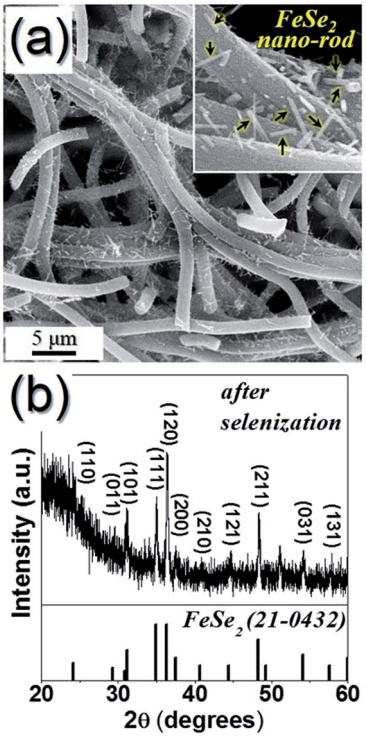

Fig. 1 Morphology and crystal structure of the 1-D nanostructure $FeSe_2$–C composite nanofibers obtained after selenization at 400 °C: (a) SEM image and (b) XRD pattern.

sizes of the 1-D nanostructures post-treated at 400, 500, and 600 °C were calculated to be 16, 28, and 39 nm, respectively. The changes in the morphology of the $FeSe_2$/C composite nanofibers during the oxidation as a function of the post-treatment temperature are shown in Fig. 2–6. During oxidation at temperatures between 400 and 600 °C, the C component in the $FeSe_2$/C composite fibers decomposed, and necking occurred between the adjacent Fe_2O_3 nanorods. Accordingly, the three samples (Sel.400-Oxi.400, Sel.400-Oxi.500, and Sel.400-Oxi.600) exhibited similar 1-D nanostructure morphologies consisting of numerous nanorods, regardless of the oxidation temperature, as shown in the SEM and low-resolution TEM images in Fig. 2. However, the high-resolution TEM (HR-TEM) images shown in Fig. 3, 5 and 6 demonstrate in further detail that the internal structure of the nanorods constituting the 1-D nanostructures varies with the oxidation temperature.

The HR-TEM images (Fig. 3a–c) of the Sel.400-Oxi.400 nanofibers revealed clear nanovoids, which were formed by nanoscale Kirkendall diffusion, embedded within the nanorods. A nanovoid that is smaller than 5 nm in diameter is shown in the inset image of Fig. 3c. The selected area electron diffraction (SAED) pattern shown in Fig. 3d revealed the mixed crystalline structure of Fe_2O_3 and metalloid Se phases. However, the Se phase with relatively small crystals was not detected in the XRD analysis in Fig. S2.† The $FeSe_2$ phase was not observed in the SAED or XRD patterns of the Sel.400-Oxi.400 nanofibers. Therefore, $FeSe_2$ completely converted into Fe_2O_3 even at the post-treatment temperature of 400 °C. The iron component of

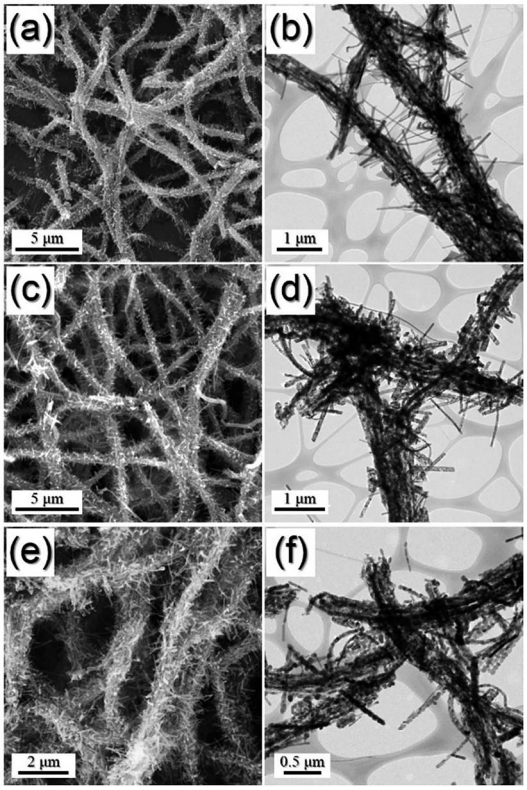

Fig. 2 Morphologies of the 1-D nanostructures comprising nanorods obtained after selenization at 400 °C and subsequent oxidation at (a and b) 400, (c and d) 500, and (e and f) 600 °C.

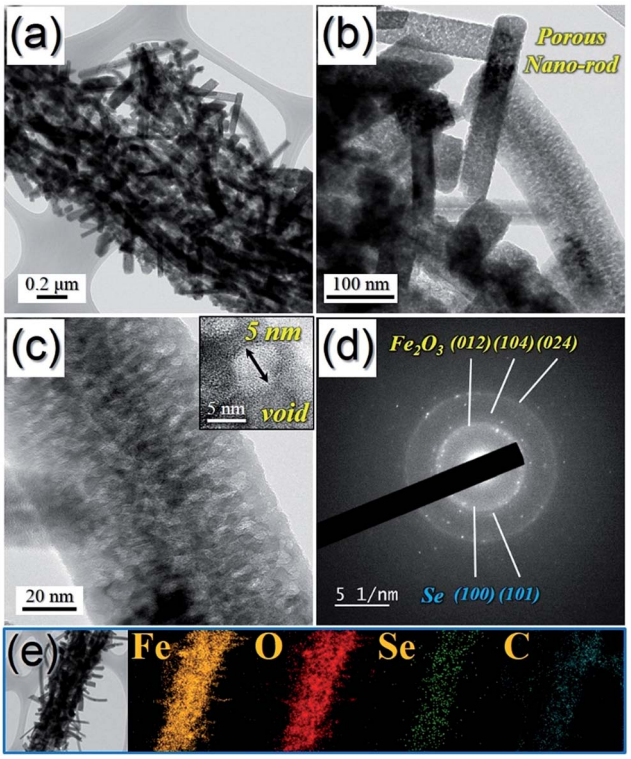

Fig. 3 Morphologies, SAED pattern, and elemental mapping images of the Sel.400-Oxi.400 nanofibers: (a and b) TEM images, (c) HR-TEM image, (d) SAED pattern, and (e) elemental mapping images.

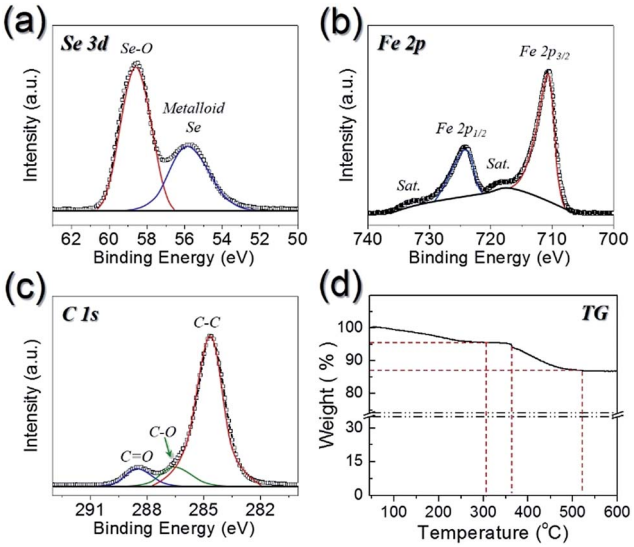

Fig. 4 XPS (a–c) and TG (d) analysis of the Sel.400-Oxi.400 nanofibers: (a) Se 3d spectrum, (b) Fe 2p spectrum, (c) C 1s spectrum, and (d) TG curve.

$FeSe_2$ moved out to the outer surface of the nanorod, where it reacted with oxygen gas to form Fe_2O_3. However, the partial removal of metalloid Se, which was formed by the different diffusion rates of Fe and Se ions during the nanoscale Kirkendall diffusion, left remaining metalloid Se within the nanorods with nanovoids. Therefore, the nanorods constituting the Sel.400-Oxi.400 nanofibers exhibited a mixed structure of crystalline Fe_2O_3 and metalloid Se phases. The elemental mapping images shown in Fig. 3e reveal the uniform distribution of metalloid Se throughout the 1-D nanostructure. Carbon was also detected in the elemental mapping image. The visible grayish color of the nanofibers also confirmed the existence of residual carbon in the Sel.400-Oxi.400 nanofibers. The incomplete elimination of metalloid Se within the nanorods was further demonstrated by the metalloid Se peak with a binding energy of 55.5 eV in the XPS Se spectrum, as shown in Fig. 4a.[30–32] The additional Se–O peak with binding energy of 58.6 eV was attributed to SeO_2 formed by reaction of diffused-out Se component and oxygen gas.[32] In the Fe 2p spectrum (Fig. 4b), the main peaks were observed at binding energies of 711.3 eV (Fe $2p_{3/2}$) and 724.1 eV (Fe $2p_{1/2}$), which are characteristic of Fe_2O_3.[30,31] Furthermore, in the C 1s XPS spectrum (Fig. 4c), peaks corresponding to sp_2-bonded carbon (C–C), epoxy and alkoxy groups (C–O), and carbonyl and carboxylic (C═O) components were observed at 284.2, 286.5, and 288.0 eV, respectively.[33] The peak corresponding to the C–C bond exhibited the highest intensity, indicating the formation of graphitic carbon. The TG curve of the Sel.400-Oxi.400 nanofibers shown in Fig. 4d showed two-step weight loss. The first-step weight loss below 310 °C was attributed to elimination of metalloid Se through SeO_2. The stepwise weight loss between 370 and 530 °C was attributed to combustion of carbon

material. The slow outward diffusion rate of metalloid Se by nanoscale Kirkendall diffusion resulted in the stepwise weight loss in the TG analysis. The sublimation temperature of SeO_2 is known as 315 °C.[34] The Se and C contents in the Sel.400-Oxi.400 nanofibers were estimated as approximately 5 and 7 wt% from the TG analysis.

The morphologies of the Sel.400-Oxi.500 nanofibers are shown in detail in Fig. 5a–c. HR-TEM images confirmed the hollow structure of the Fe_2O_3 nanorods formed by the complete conversion of $FeSe_2$ into Fe_2O_3 and the elimination of metalloid Se through nanoscale Kirkendall diffusion. The diameter of the Fe_2O_3 nanorod and the corresponding shell thickness were about 48 and 15 nm, respectively, as determined from the TEM image shown in Fig. 5c. The inset HR-TEM image shown in Fig. 5c revealed clear lattice fringes separated by 0.252 nm, which correspond to the (110) crystal plane of the hexagonal Fe_2O_3 phase. The SAED and XRD patterns and the TG curve shown in Fig. 5d, S2 and S3a,† respectively, also revealed the formation of phase-pure Fe_2O_3 nanorods without impurities. Se and C were not observed in the elemental mapping images shown in Fig. 5e.

The densification and sintering of the hollow Fe_2O_3 nanorod nanostructure occurred at the highest oxidation temperature of 600 °C, as shown in Fig. 6a–c. The hollow Fe_2O_3 nanorods shrank and densified, which slightly decreased the mean thickness of the nanorods constituting the Sel.400-Oxi.600 nanofibers. The thickness of the Fe_2O_3 nanorods after oxidation at 600 °C was about 40 nm in Fig. 6c. The HR-TEM image

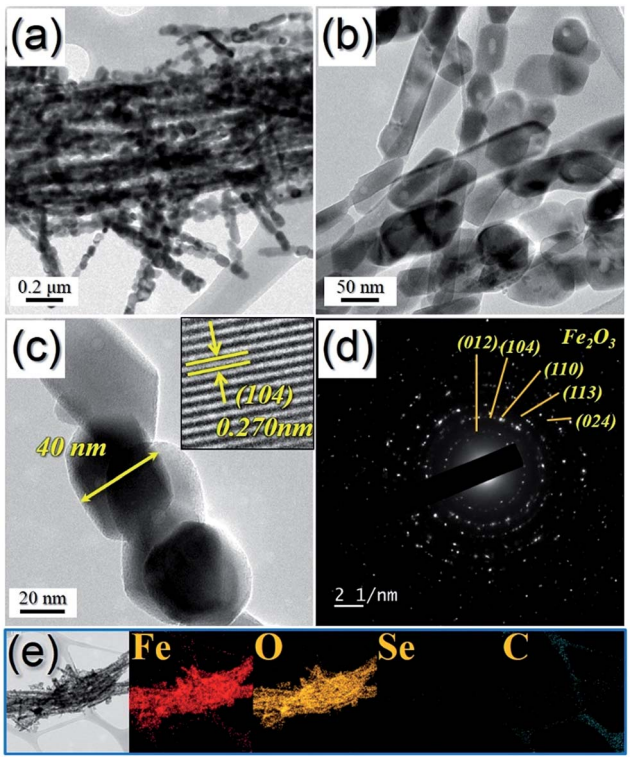

Fig. 6 Morphologies, SAED pattern, and elemental mapping images of the Sel.400-Oxi.600 nanofibers: (a and b) TEM images, (c) HR-TEM image, (d) SAED pattern, and (e) elemental mapping images.

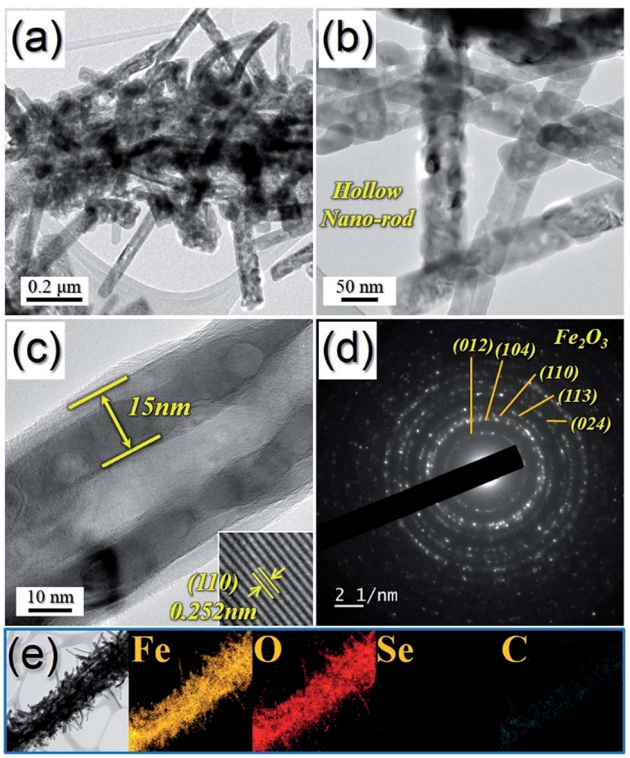

Fig. 5 Morphologies, SAED pattern, and elemental mapping images of the Sel.400-Oxi.500 nanofibers: (a and b) TEM images, (c) HR-TEM image, (d) SAED pattern, and (e) elemental mapping images.

demonstrated the well-faceted crystal structure and the clear lattice fringes separated by 0.270 nm corresponding to the (104) lattice plane of hexagonal Fe_2O_3, as shown in Fig. 6d. The SAED and XRD patterns and the TG curve shown in Fig. 6d, S2 and S3b,† respectively, also revealed the formation of phase-pure Fe_2O_3 nanorods with high crystallinity. Similar to the results of Sel.400-Oxi.500 nanofibers, Se and C were not observed in the elemental mapping images shown in Fig. 6e. The BET surface areas of the nanorod nanostructures obtained after selenization at 400 °C and subsequent oxidation at 400, 500, and 600 °C were 39, 73, and 29 $m^2\ g^{-1}$, respectively (Fig. S4†). The complete elimination of metalloid Se increased the BET surface area of the Sel.400-Oxi.500 nanofibers. However, densification during sintering decreased the BET surface area of the Sel.400-Oxi.600 nanofibers.

The electrochemical properties of the three 1-D nanostructures, *i.e.*, the porous Fe_2O_3/Se composite (Sel.400-Oxi.400) and the hollow and dense pure Fe_2O_3 nanorods (Sel.400-Oxi.500 and Sel.400-Oxi.600, respectively) for Li^+ ion storage are shown in Fig. 7. The normalized CV curves of Sel.400-Oxi.400 are compared with those of Sel.400-Oxi.500 and Sel.400-Oxi.600 for the first five cycles at a scan rate of 0.07 mV s^{-1} in the 0.001–3.0 V range, as shown in Fig. 7a and b and S5a.† A distinct reduction peak at around 0.7 V is observed in the first cathodic sweep of the three samples due to the reduction of Fe_2O_3 to metallic Fe and the formation of amorphous Li_2O, as well as the decomposition of organic electrolyte to form a solid electrolyte interphase (SEI) layer.[35–37] However, an extra reduction peak at

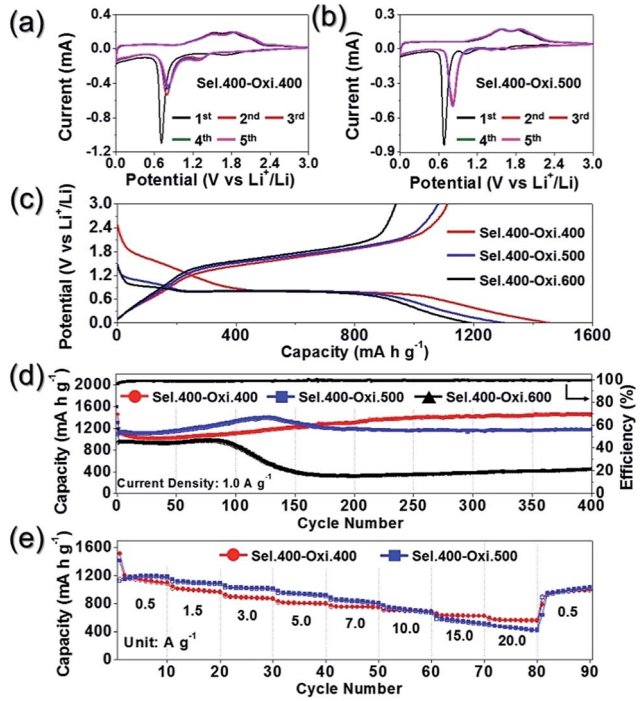

Fig. 7 Electrochemical properties of the 1-D nanostructures comprising porous Fe_2O_3/Se composite, hollow and dense Fe_2O_3 nano-rods (Sel.400-Oxi.400, Sel.400-Oxi.500, and Sel.400-Oxi.600): (a) CV curves of the Sel.400-Oxi.400, (b) CV curves of the Sel.400-Oxi.500, (c) first discharge–charge curves at a current density of 1.0 A g^{-1}, (d) cycling performances and coulombic efficiencies of Sel400-Oxi.400, and (e) rate performances.

1.8 V was only observed for the Sel.400-Oxi.400 sample due to the formation of Li_2Se through the reduction of metalloid Se in the porous Fe_2O_3/Se nanorod structure.[38] During the charging process, oxidation of Fe into Fe_3O_4 and Fe_3O_4 into Fe_2O_3 occurred at around 1.6 and 1.8 V, respectively, in both the Fe_2O_3 and porous Fe_2O_3/Se nanorod structures. Also, during charging, Fe was selenized to $FeSe_x$ at around 1.8 V in case of the porous Fe_2O_3/Se nanorod structures.[38–41] However, it was difficult to distinguish the peak for selenization of Fe to $FeSe_x$ from the CV curves. From the second cycle onward for Sel.400-Oxi.400, the peak at 1.8 V disappeared, and a new reduction peak emerged at 1.3 V. The new reduction peak was attributed to the reduction of $FeSe_x$, which formed due to the reaction of monocrystalline Fe and Li_2Se.[38] Therefore, the electrochemical reaction mechanism of the Fe_2O_3/Se nanorod structure for Li-ion storage can be summarized as follows.

First discharge process:

$$Fe_2O_3 + 6Li^+ + 6e^- \rightarrow 2Fe + 3Li_2O \quad (1)$$

$$Se + 2Li^+ + 2e^- \rightarrow Li_2Se \quad (2)$$

Charge process:

$$Fe + xLi_2Se \rightarrow FeSe_x + xLi^+ + xe^- \quad (3)$$

$$2Fe + 3Li_2O \rightarrow Fe_2O_3 + 6Li^+ + 6e^- \quad (4)$$

Subsequent discharge processes:

$$Fe_2O_3 + 6Li^+ + 6e^- \rightarrow 2Fe + 3Li_2O \quad (5)$$

$$FeSe_x + xLi^+ + xe^- \rightarrow Fe + xLi_2Se \quad (6)$$

The main reduction peak at around 0.7 V of the three samples shifts to a slightly higher potential after the first cycle due to the formation of ultrafine nanocrystals during the first cycle.[42,43] From the third cycle onward, all reduction and oxidation peaks of three samples remained unchanged, indicating the good reversibility of the electrochemical reactions.

The results of the initial discharge and charge curves obtained at a current density of 1.0 A g^{-1} shown in Fig. 7c were in good agreement with those of the CV curves. A long plateau at approximately 0.7 V appeared in the initial discharge curves of all three samples due to the reduction of Fe_2O_3 to metallic Fe. The nanostructure composed of the porous Fe_2O_3/Se composite nanorods exhibited an extra plateau at approximately 1.8 V in the initial discharge curve because of the formation of Li_2Se through the reduction of metalloid Se. The two 1-D nanostructures comprising pure Fe_2O_3 nanorods (Sel.400-Oxi.500 and Sel.400-Oxi.600) exhibited similar curve shapes, irrespective of their morphologies. The initial discharge capacities of Sel.400-Oxi.400, Sel.400-Oxi.500, and Sel.400-Oxi.600 were 1458, 1303, and 1193 mA h g^{-1}, respectively, and their corresponding charge capacities were 1112, 1080, and 938 mA h g^{-1}, respectively. The Sel.400-Oxi.400 nanofibers showed the highest initial discharge and charge capacities due to their unique architecture containing numerous nanovoids under 5 nm in diameter at a high current density of 1.0 A g^{-1}.

The cycling performance of the three samples at a constant current density of 1.0 A g^{-1} is shown in Fig. 7d. The 1-D nanostructures composed of porous and hollow nanorods (Sel.400-Oxi.400 and Sel.400-Oxi.500, respectively) exhibited superior cycling performance to that of the 1-D nanostructure comprising dense nanorods (Sel.400-Oxi.600). The structural degradation caused by repeated Li insertion/deinsertion in the Sel.400-Oxi.600 nanofibers sharply decreased the discharge capacities after 100 cycles. The discharge capacities of Sel.400-Oxi.400 and Sel.400-Oxi.500 increased during the first 370 and 128 cycles, respectively. The discharge capacities of Sel.400-Oxi.400, Sel.400-Oxi.500, and Sel.400-Oxi.600 during the 400th cycle were 1456, 1187, and 458 mA h g^{-1}, respectively. The theoretical capacity of Fe_2O_3 as anode material for lithium ion battery is *ca.* 1005 mA h g^{-1}. The extra capacities of Sel.400-Oxi.400, Sel.400-Oxi.500 may be due to the reversible growth of the polymeric gel-like film by the kinetically activated electrolyte degradation of alkyl carbonate electrolytes.[44–46] The initial coulombic efficiency of Sel400-Oxi.400 was 76%, and it increased quickly, close to an average value of 99% in the following cycles in Fig. 7d. The rate performances of the porous Fe_2O_3/Se and hollow Fe_2O_3 nanorod nanostructures are shown in Fig. 7e, with the current density increasing stepwise from 0.2 to 20.0 A g^{-1} and with 10 cycles performed at each step. The two types of nanofibers exhibited excellent rate performances. The uniquely structured nanorods with numerous nanovoids (~5 nm) and hollow inner spheres

decreased the diffusion distance and increased the diffusion rate of Li^+ ions. Moreover, FeSe, which has a higher electrical conductivity than that of Fe_2O_3, formed during charge–discharge process, thus enhancing the rate property of the porous Fe_2O_3/Se nanorod nanostructure (Sel.400-Oxi.400). The final rate capacities of the 1-D nanostructures with porous Fe_2O_3/Se nanorods were 1094, 959, 872, 796, 747, 696, 624, and 553 mA h g^{-1} at current densities of 0.5, 1.5, 3.0, 5.0, 7.0, 10.0, 15.0, and 20.0 A g^{-1}, respectively. The discharge capacities of the Sel.400-Oxi.400 and Sel.400-Oxi.500 nanofibers recovered well to 1002 mA h g^{-1} as the current density returned to 0.5 A g^{-1} after 80 cycles at high current densities.

EIS was carried out to explain the superior cycling and rate performances of the 1-D nanostructures with porous Fe_2O_3/Se nanorods. The Nyquist impedance plots of the samples obtained before and after cycling under a fully charged state are shown in Fig. 8. The medium-frequency semicircles in the Nyquist plots of the electrodes are assigned to the charge-transfer resistance (R_{ct}).[47–49] The porous Fe_2O_3/Se and dense Fe_2O_3 nanorod nanostructures exhibited lower R_{ct} values of 49 and 51 Ω than that of hollow Fe_2O_3 nanorods (68 Ω) before cycling, as shown in Fig. 8a. The metalloid Se and graphitic carbon with high electrical conductivities in Fe_2O_3–Se and high crystallinity of dense Fe_2O_3 nanorods resulted in low R_{ct} values before cycling. The R_{ct} values of the three samples decreased after the first cycle owing to the formation of an amorphous structure, as shown in Fig. 8b–d. The R_{ct} values of the porous Fe_2O_3/Se nanorod nanostructure changed slightly from 15 Ω during the 50th cycle to 18 Ω during the 200th cycle, as shown in Fig. 8b. However, the R_{ct} value of the dense Fe_2O_3 nanorod nanostructure increased abruptly from 17 Ω to 46 Ω from the 50th to the 200th cycle due to the structural destruction during repeated Li^+ ion insertion and deinsertion processes, as shown in Fig. 8d. The electrochemical properties of the 1-D nanostructure composed of porous Fe_2O_3/Se composite nanorods were compared with those of the nanostructured iron oxide and chalcogenide materials reported in the literatures, and the results were summarized in Tables S1 and S2.† The Fe_2O_3 anode materials without carbon contents had low discharge capacities in spite of short cycle numbers. However, the 1-D nanostructure composed of porous Fe_2O_3/Se composite nanorods prepared in this study showed superior electrochemical properties for lithium-ion storage compared to those of other Fe related materials reported in the literatures even at a higher current density. Thus, the unique porous architecture not only offers the advantages of 1-D nanostructures but also effectively accommodates the volume changes of Fe_2O_3 due to its nanovoids. This structure also decreases the diffusion distance of Li^+ ions and increases the diffusion rate of Li^+ ions during the cycling process. The metalloid Se phase and the resulting $FeSe_x$ formed during cycling improved the electrical conductivity of the Fe_2O_3 in porous Fe_2O_3/Se composite nanostructure. Therefore, this nanostructure resulted in superior electrochemical properties during long-term cycling.

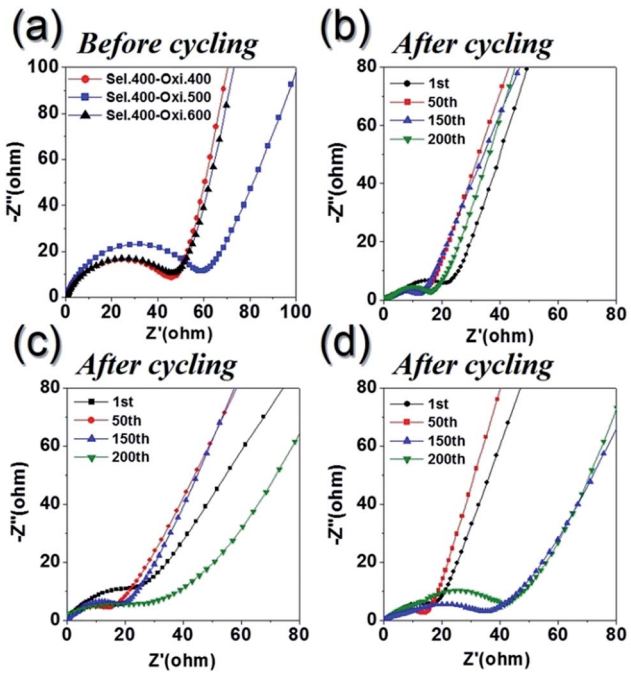

Fig. 8 Nyquist impedance plots of the 1-D nanostructures comprising porous Fe_2O_3/Se composite, hollow and dense Fe_2O_3 nano-rods (Sel.400-Oxi.400, Sel.400-Oxi.500, and Sel.400-Oxi.600): (a) before and after cycling of (b) Sel.400-Oxi.400, (c) Sel.400-Oxi.500, and (d) Sel.400-Oxi.600.

Conclusions

Novel 1-D nanostructures, one comprising a porous Fe_2O_3/Se composite and the other comprising subsequently formed hollow Fe_2O_3 nanorods, were prepared by exploiting a nanoscale Kirkendall diffusion mechanism during post-treatment after the electrospinning process. The different diffusion rates of Fe and Se ions and oxygen gas in the structure led to Kirkendall diffusion, which is a key factor in the formation of the Fe_2O_3/Se composite and hollow Fe_2O_3 nanorod nanostructures. The porous Fe_2O_3/Se nanorod nanostructure exhibited superior electrochemical properties for Li-ion storage by improving the structural stability and electrical conductivity during repeated Li insertion/deinsertion processes. This facile synthetic method could be widely applied in the design and synthesis of novel intermetallic compounds in various applications, such as catalysis, gas sensors, and hydrogen evolution reactions, as well as anode materials for LIBs.

Acknowledgements

This work was supported by the National Research Foundation of Korea (NRF) grant funded by the Korea government (MEST) (No. NRF-2015R1D1A1A01058979).

References

1 Y. P. Zhu, T. Y. Ma, M. Jaroniec and S. Z. Qiao, *Angew. Chem., Int. Ed. Engl.*, 2017, **56**, 1324–1328.
2 A. D. Roberts, X. Li and H. Zhang, *Chem. Soc. Rev.*, 2014, **43**, 4341–4356.

3 W. Yuan, Y. Tang, X. Yang and Z. Wan, *Appl. Energy*, 2012, **94**, 309–329.
4 L. Zhou, Z. Li, Z. Liu, M. Yin, J. Ren and X. Qu, *Nanoscale*, 2014, **6**, 1445–1452.
5 L. Zhou, Z. Zhuang, H. Zhao, M. Lin, D. Zhao and L. Mai, *Adv. Mater.*, 2017, DOI: 10.1002/adma.201602914.
6 B. Braunecker and P. Simon, *Phys. Rev. Lett.*, 2013, **111**, 147202.
7 T. Ling, D. Y. Yan, Y. Jiao, H. Wang, Y. Zheng, X. Zheng, J. Mao, X. W. Du, Z. Hu, M. Jaroniec and S. Z. Qiao, *Nat. Commun.*, 2016, **7**, 12876.
8 E. Yeganegi, A. Lagendijk, A. P. Mosk and W. L. Vos, *Phys. Rev. B: Condens. Matter Mater. Phys.*, 2014, **89**, 045123.
9 Y. Zhou, L. Wang, S. Chen, S. Qin, X. Liu, J. Chen, D.-J. Xue, M. Luo, Y. Cao and Y. Cheng, *Nat. Photonics*, 2015, **9**, 409–415.
10 X. Zhang, H. Chen, Q. Y. Xie and J. Guo, *J. Mater. Chem. A*, 2014, **2**, 3912–3918.
11 J. Guo, H. Zhu, Y. Sun and X. Zhang, *J. Mater. Chem. A*, 2015, **3**, 19384–19392.
12 J. L. Xie, C. X. Guo and C. M. Li, *Energy Environ. Sci.*, 2014, **7**, 2559–2579.
13 X. Yu, Y. Fu, X. Cai, H. Kafafy, H. Wu, M. Peng, S. Hou, Z. Lv, S. Ye and D. Zou, *Nano Energy*, 2013, **2**, 1242–1248.
14 C. Zhu, X. Mu, P. A. van Aken, Y. Yu and J. Maier, *Angew. Chem., Int. Ed. Engl.*, 2014, **53**, 2152–2156.
15 J. S. Cho, Y. J. Hong and Y. C. Kang, *ACS Nano*, 2015, **9**, 4026–4035.
16 H. Liu, S. Chen, G. Wang and S. Z. Qiao, *Chem.–Eur. J.*, 2013, **19**, 16897–16901.
17 J. Liu, Z. Yang, J. Wang, L. Gu, J. Maier and Y. Yu, *Nano Energy*, 2015, **16**, 389–398.
18 J. Liu, L. Yu, C. Wu, Y. Wen, K. Yin, F.-K. Chiang, R. Hu, J. Liu, L. Sun and L. Gu, *Nano Lett.*, 2017, **17**, 2034–2042.
19 L. Shen, L. Yu, X. Y. Yu, X. Zhang and X. W. D. Lou, *Angew. Chem., Int. Ed. Engl.*, 2015, **54**, 1868–1872.
20 J. S. Cho and Y. C. Kang, *Small*, 2015, **11**, 4673–4681.
21 Y. J. Hong, J. W. Yoon, J. H. Lee and Y. C. Kang, *Chem.–Eur. J.*, 2015, **21**, 371–376.
22 W. Li, M. Li, M. Wang, L. Zeng and Y. Yu, *Nano Energy*, 2015, **13**, 693–701.
23 Y.-E. Miao, Y. Huang, L. Zhang, W. Fan, F. Lai and T. Liu, *Nanoscale*, 2015, **7**, 11093–11101.
24 Y. Yu, L. Gu, C. Wang, A. Dhanabalan, P. A. van Aken and J. Maier, *Angew. Chem., Int. Ed. Engl.*, 2009, **48**, 6485–6489.
25 J. Chen, L.-N. Xu, W.-Y. Li and X.-L. Gou, *Adv. Mater.*, 2005, **17**, 582–586.
26 C. T. Cherian, J. Sundaramurthy, M. Kalaivani, P. Ragupathy, P. S. Kumar, V. Thavasi, M. Reddy, C. H. Sow, S. G. Mhaisalkar and S. Ramakrishna, *J. Mater. Chem.*, 2012, **22**, 12198–12204.
27 S. Chaudhari and M. Srinivasan, *J. Mater. Chem.*, 2012, **22**, 23049–23056.
28 S. Xu, C. M. Hessel, H. Ren, R. Yu, Q. Jin, M. Yang, H. Zhao and D. Wang, *Energy Environ. Sci.*, 2014, **7**, 632–637.
29 X. Xu, R. Cao, S. Jeong and J. Cho, *Nano Lett.*, 2012, **12**, 4988–4991.
30 J. S. Cho, J.-K. Lee and Y. C. Kang, *Sci. Rep.*, 2016, **6**, 23699.
31 S. Huang, Q. He, W. Chen, J. Zai, Q. Qiao and X. Qian, *Nano Energy*, 2015, **15**, 205–215.
32 G. D. Park, J. K. Lee and Y. C. Kang, *Adv. Funct. Mater.*, 2016, **27**, 1603399–1603408.
33 J. S. Cho, J. M. Won, J.-K. Lee and Y. C. Kang, *Nano Energy*, 2016, **26**, 466–478.
34 A. C. Maity, *Synlett*, 2008, **2008**, 465–466.
35 C. K. Chan, H. Peng, G. Liu, K. McIlwrath, X. F. Zhang, R. A. Huggins and Y. Cui, *Nat. Nanotechnol.*, 2008, **3**, 31–35.
36 S. Ni, X. Yang and T. Li, *J. Mater. Chem.*, 2012, **22**, 2395–2397.
37 X. Yan, X. Tong, J. Wang, C. Gong, M. Zhang and L. Liang, *Mater. Lett.*, 2014, **136**, 74–77.
38 W.-J. Li, Y.-N. Zhou and Z.-W. Fu, *Electrochim. Acta*, 2010, **55**, 8680–8685.
39 G. Gao, L. Yu and H. B. Wu, *Small*, 2014, **10**, 1741–1745.
40 W. M. Zhang, X. L. Wu, J. S. Hu, Y. G. Guo and L. J. Wan, *Adv. Funct. Mater.*, 2008, **18**, 3941–3946.
41 Y. Zhao, J. Li, Y. Ding and L. Guan, *Chem. Commun.*, 2011, **47**, 7416–7418.
42 J. S. Cho, J. M. Won, J.-H. Lee and Y. C. Kang, *Nanoscale*, 2015, **7**, 19620–19626.
43 Y. Sun, X. Hu, W. Luo, F. Xia and Y. Huang, *Adv. Funct. Mater.*, 2013, **23**, 2436–2444.
44 J. Bai, X. Li, G. Liu, Y. Qian and S. Xiong, *Adv. Funct. Mater.*, 2014, **24**, 3012–3020.
45 L. Su, Y. Zhong and Z. Zhou, *J. Mater. Chem. A*, 2013, **1**, 15158–15166.
46 L. Zhou, D. Zhao and X. W. Lou, *Adv. Mater.*, 2012, **24**, 745–748.
47 D. T. Ngo, R. S. Kalubarme, H. T. Le, J. G. Fisher, C. N. Park, I. D. Kim and C. J. Park, *Adv. Funct. Mater.*, 2014, **24**, 5291–5298.
48 Z. Wang, D. Luan, S. Madhavi, Y. Hu and X. W. D. Lou, *Energy Environ. Sci.*, 2012, **5**, 5252–5256.
49 Y. Xu, Y. Zhu, Y. Liu and C. Wang, *Adv. Energy Mater.*, 2013, **3**, 128–133.